# Precise response functions in all-electron methods: Generalization to nonspherical perturbations and application to NiO

Markus Betzinger,* Christoph Friedrich, and Stefan Blügel
*Peter-Grünberg Institut and Institute for Advanced Simulation, Forschungszentrum Jülich and JARA, D-52425 Jülich, Germany*
(Received 22 May 2013; published 19 August 2013)

In a previous publication [Betzinger, Friedrich, Görling, and Blügel, Phys. Rev. B **85**, 245124 (2012)] we presented a technique to compute accurate all-electron response functions, e.g., the density response function, within the full-potential linearized augmented-plane-wave (FLAPW) method. Response contributions that are not captured (completely) within the finite Hilbert space spanned by the LAPW basis are taken into account by an incomplete-basis-set correction (IBC). The latter is based on a formal response of the basis functions themselves, which is derived by exploiting their dependence on the effective potential. Its construction requires the solution of radial differential equations, having the form of Sternheimer equations, by numerical integration. The approach includes a formally exact treatment of the response contribution from the core states. While we restricted the formalism to spherical perturbations in the previous work, we here generalize the formalism to nonspherical perturbations. The improvements are demonstrated with exact-exchange optimized-effective-potential (EXX-OEP) calculations of antiferromagnetic NiO. It is shown that with the generalized IBC a basis-set convergence is realized that is as fast as in density-functional theory calculations using standard local or semilocal functionals. The EXX-OEP band gap, magnetic moment, and spectral function of NiO are in substantially better agreement with experiment than results obtained from calculations with local and semilocal functionals.

DOI: 10.1103/PhysRevB.88.075130 PACS number(s): 71.15.Mb, 71.45.Gm, 71.27.+a

## I. INTRODUCTION

Over recent decades, linear response theory based on Kohn-Sham density-functional theory (KS-DFT)[1–3] has evolved to a powerful numerical approach in solid state physics for calculating the response of a system due to an external perturbation, which may arise, for example, from an atomic displacement giving rise to lattice vibrations or from an external electric field leading to the electric-field response of the material.[4] Furthermore, response quantities are often central ingredients in electronic structure methods that go beyond standard DFT. For example, the adiabatic-connection fluctuation-dissipation theorem[5,6] as well as the $GW$ approximation[7,8] for the electronic self-energy involve the frequency- and momentum-dependent density response function within the random-phase approximation (RPA). The inverse of its static limit enters the optimized-effective-potential (OEP) approach of KS-DFT[9,10] where an effective local potential is constructed from a general orbital-dependent exchange-correlation (xc) functional.

In all cases, the linear change of the KS single-particle wave functions due to a perturbing potential has to be calculated. By expressing the linear response in the complete space of the KS eigenstates, one obtains an exact expression written as an infinite sum over the unperturbed eigenstates, a well known result from quantum mechanics textbooks.

In a practical calculation, of course, only a finite number of states are available, leading to a loss of accuracy. It is a matter of experience that the response function converges very slowly with respect to the number of states taken into account. Furthermore, the calculated KS wave functions, especially those at high energies, deviate from the true physical eigenstates due to the incompleteness of the basis set, which also has an adverse effect on the accuracy of the sum-over-states expression. These issues are particularly problematic in minimal basis sets that are optimized for representing the occupied single-particle states. Examples are the linearized muffin-tin orbital (LMTO)[11,12] and the full-potential linearized augmented-plane-wave (FLAPW) method.[13–15] Only a relatively small number of empty states are available in these methods, and only the lower lying ones are accurate representations of the true eigenstates. The majority of linear response calculations have been performed within the pseudopotential plane-wave method[16,17] so far, where much larger basis sets are employed.

Recently,[18] we presented an incomplete-basis-set correction (IBC) for the calculation of response functions in the FLAPW method, which tremendously accelerates the convergence in terms of the basis set and the number of unoccupied states. The IBC corrects (1) for the truncation of the sum-over-states expression and (2) for the deviations in the calculated wave functions from the true pointwise solutions of the KS equation. In order to give a simple picture of the IBC we remind the reader of the basic construction principle of the LAPW basis functions in the atomic muffin-tin (MT) spheres: There, one employs functions that are pointwise solutions of the KS equation with the spherical part of the effective potential. These basis functions can already be regarded as approximate solutions to the underlying KS equation and thus form a very accurate basis set. In the IBC, we adopt this principle for the linear response: By solving radial Sternheimer equations[19] we construct the linear response of the basis functions in terms of a perturbation in the potential, yielding the *exact* response for the spherical problem, which already gives the main contribution to the response for the full-potential case. Through the *exact* response, an infinite number of empty states is incorporated in principle. The seeming disadvantage of the minimal LAPW basis set is thus turned into an advantage.

We note in passing that the present method should not be mistaken with the Sternheimer approach,[4] usually used in the pseudopotential plane-wave method, which replaces the sum-over-states expression by the identical solution

 

to the inhomogeneous differential Sternheimer equation in a basis set. In contrast to the present IBC method, the Sternheimer approach does not account for corrections due to the incompleteness of the basis set. In other words, response contributions that lie outside the space spanned by the basis set are lost.

For simplicity, we restricted in Ref. 18 the formalism of the IBC to *spherical* perturbations, which have the beneficial property that the corresponding response of a basis function of angular momentum $l$ and magnetic quantum number $m$ stays in the same $lm$ channel as the unperturbed function. This is no longer the case for nonspherical perturbations. If, e.g., the perturbation has a shape like a $p$ function, it will raise or lower the angular quantum number of a function by 1: a $d$ function will acquire $p$ and $f$ orbital character; the $lm$ channels become coupled.

In this work, we extend our original formulation of the IBC to nonspherical perturbations in the MT spheres. Fortunately, many of the equations derived in Ref. 18 remain valid. We only have to generalize the basis response, which becomes a vector quantity in the $lm$ quantum numbers. Furthermore, we have to find a new treatment for the response of the core states because the finite-difference approach chosen for purely spherical perturbations is no longer applicable, as our core Dirac solvers do not allow for nonspherical potentials. As a solution, we solve the inhomogeneous radial Sternheimer equations with the additional boundary condition that the core-state response goes to zero for large distances from the nucleus.

As a proof of principle, we apply the generalized IBC to the exact-exchange (EXX) OEP approach, in which a local effective potential is constructed from the self-interaction free orbital-dependent EXX functional. The local effective potential is given as the solution of an integral equation whose central ingredients are response functions for the electron density and the KS single-particle wave functions. While we demonstrated in Ref. 18 that the IBC for spherical perturbations already improves EXX-OEP calculation in terms of numerical stability and computational efficiency for a wide range of materials, we show here that for complex materials such as antiferromagnetic NiO, whose electronic density is strongly anisotropic, the generalized IBC is essential and leads to a basis-set convergence behavior similar to calculations with standard xc functionals such as the LDA or GGA. Furthermore, very few empty states are needed to converge the response quantities.

The paper is organized as follows. In Sec. II we give a short recapitulation of the IBC and derive its generalization for nonspherical perturbations. In Sec. III we apply the IBC to the EXX-OEP approach and analyze the effect of the generalized IBC on the convergence of the KS density response function, the EXX potential, and the KS EXX gap in detail. The electronic structure of antiferromagnetic NiO as obtained by the EXX-OEP method is discussed in Sec. IV. Finally, we draw our conclusions in Sec. V.

## II. INCOMPLETE-BASIS-SET CORRECTION

As already mentioned, the generalized derivation of the IBC follows very closely the one developed in Ref. 18 for the spherical perturbations. Therefore, we recapitulate this derivation in Sec. II A and extend the formalism whenever necessary to the more general case of nonspherical perturbations in the effective potential. In Sec. II B we then discuss the calculation of the core-state response, which requires a more sophisticated treatment than for purely spherical perturbations. When referring to equations of Ref. 18 we use a prime ($'$). Unless noted otherwise, we employ the same notation, definitions, and units (i.e., Hartree atomic units). For simplicity, the spin index is suppressed and we restrict the discussion to the nonrelativistic equations. The numerical implementation, however, uses the corresponding scalar-relativistic equations.

### A. Generalization

We want to calculate the response $\varphi^{(1)}_{n\mathbf{k},I}(\mathbf{r})$ of a KS single-particle wave function $\varphi_{n\mathbf{k}}(\mathbf{r})$ in terms of a perturbation $M_I(\mathbf{r})$ [Eq. (19′)], where the latter is a function of the mixed product basis (MPB) set $\{M_I(\mathbf{r})\}$.[20–22] While in Ref. 18 we restricted the formalism to spherically symmetric functions $M_I(\mathbf{r}) = M_I(r)$, we now allow generally for nonspherical perturbations $M_I(\mathbf{r}) = M_I(r)Y_{LM}(\hat{\mathbf{r}})$ given as a product of radial function $M_I(r)$ and spherical harmonic $Y_{LM}(\hat{\mathbf{r}})$ with the composite index $I = (a,P,L,M)$, where $a$ is the atomic index and $P$ distinguishes between different radial functions $M_I(r) = M^a_{PL}(r)$. The latter do not depend on the magnetic quantum number $M$. With the azimuthal and magnetic quantum numbers $L$ and $M$ we can realize general angular dependent perturbations in the MT sphere, including spherical perturbations as the special case $L = M = 0$.

When representing $\varphi_{n\mathbf{k}}(\mathbf{r})$ in terms of the LAPW basis [Eq. (8′)], the functional derivative in Eq. (19′) will produce one term where the basis functions themselves are differentiated [Eq. (24′)]. In the MT spheres, the basis functions Eq. (9′) depend, in fact, on the potential through the functions $u^a_{lmp}(\mathbf{r}) = u^a_{lp}(r)Y_{lm}(\hat{\mathbf{r}})$ defined in Eqs. (12′) and (14′). The linear response of the latter due to a spherical perturbation $M_I(\mathbf{r}) = M_I(r)$ given by Eqs. (26′) and (27′) remains in the same $lm$ channel as the original function, i.e., $u^{a(1)}_{lmp,I}(\mathbf{r}) = u^{a(1)}_{lp,I}(r)Y_{lm}(\hat{\mathbf{r}})$. A nonspherical perturbation $M_I(\mathbf{r}) = M_I(r)Y_{LM}(\hat{\mathbf{r}})$ with $L > 0$, however, creates response contributions in more than one $lm$ channel. The total response of $u^a_{lmp}(\mathbf{r})$ is thus given generally as a sum over spherical harmonics,

$$u^{a(1)}_{lmp,I}(\mathbf{r}) = \sum_{l'm'} u^{a(1)}_{lmp,I,l'm'}(r)Y_{l'm'}(\hat{\mathbf{r}})\,, \tag{1}$$

whose radial parts obey inhomogeneous differential equations derived in the framework of Rayleigh-Schrödinger perturbation theory for degenerate states. Instead of Eq. (26′), the response of the radial basis function for $p = 0$ is given by

$$\left[h^a_{l'} - \epsilon^a_l\right] r u^{a(1)}_{lm0,I,l'm'}(r) = G^{Mm'm}_{Ll'l}\left[\delta_{ll'}\epsilon^{a(1)}_{l,I} - M_I(r)\right] r u^a_{l0}(r)\,, \tag{2}$$

and Eq. (27′), the response of the energy derivative ($p = 1$), is replaced by

$$\left[h^a_{l'} - \epsilon^a_l\right] r u^{a(1)}_{lm1,I,l'm'}(r) = G^{Mm'm}_{Ll'l}\left[\delta_{ll'}\epsilon^{a(1)}_{l,I} - M_I(r)\right] r u^a_{l1}(r) + r u^{a(1)}_{lm0,I,l'm'}(r) \tag{3}$$

with the Gaunt coefficients $G^{Mm'm}_{Ll'l}=\int Y_{LM}(\hat{\mathbf{r}})Y^*_{l'm'}(\hat{\mathbf{r}})Y_{lm}(\hat{\mathbf{r}})d\Omega$. For the linear change $\epsilon^{a(1)}_{l,I}$ of the energy parameter we employ the expectation value Eq. (28′). Equations (2) and (3) become identical to Eqs. (26′) and (27′) in the case of a spherical perturbation $M_I(\mathbf{r}) = M_I(r)/\sqrt{4\pi}$; note that $Y_{00}(\hat{\mathbf{r}}) = 1/\sqrt{4\pi}$. Fortunately, we do not have to evaluate Eqs. (2) and (3) for all combinations of the $lm$, $l'm'$, and $LM$ channels. First, the Gaunt coefficients are zero unless the conditions $l + l' + L$ is even, $|l - l'| \leqslant L \leqslant l + l'$, and $m - m' + M = 0$ are fulfilled, which reduces the nonzero terms in Eq. (1) to just a few; e.g., for a $p$-like perturbation a $d$ function acquires $p$ and $f$ character. Furthermore, Eqs. (2) and (3) depend on $m$, $m'$, and $M$ only through the factor $G^{Mm'm}_{Ll'l}$. Since the differential equations are linear, we only have to solve them for each $l$, $l'$, and $L$ and then scale the solution by $G^{Mm'm}_{Ll'l}$ to account for the $m$, $m'$, and $M$ dependence. As a result, Eqs. (2) and (3) have to be integrated just a few times, leading to a negligible computational cost.

The differential equations above do not determine the response $u^{a(1)}_{lmp,I,l'm'}(r)$ uniquely since we may always add a multiple of the homogeneous solution of

$$\left[h^a_{l'} - \epsilon^a_l\right] r u^{a,\mathrm{hom}}_{l,l'}(r) = 0\,. \tag{4}$$

To make the response unique, we require it to be orthogonal to the homogeneous solutions

$$\int dr\, r^2\, u^{a,\mathrm{hom}}_{l,l'}(r) u^{a(1)}_{lmp,I,l'm'}(r) = 0\,, \tag{5}$$

which ensures that a mere rigid shift of the potential to higher or lower energies (constant perturbation) leaves the wave functions unchanged. Equations (2), (3), and (4) are solved using the same radial integrators as employed to determine the radial basis functions $u^a_{lp}(r)$.

A change in the functions $u^a_{lmp}(\mathbf{r})$ also affects the matching coefficients $A^a_{lmp}(\mathbf{k},\mathbf{G})$ in Eq. (9′). In Ref. 18, we explicitly differentiated the coefficients $A^a_{lmp}(\mathbf{k},\mathbf{G})$ [given in Eq. (10′)] with respect to the spherical part of the effective potential yielding $A^{a(1)}_{lmp,I}(\mathbf{k},\mathbf{G})$ [Eq. (31′)]. For the more general case of a nonspherical perturbation we determine the change in the matching coefficients differently, because a straightforward differentiation would be very complicated. We exploit the fact that upon perturbing the potential in the MT spheres (1) the interstitial (potential independent) plane waves remain unaffected and (2) the matching at the MT sphere boundaries must preserve continuity in value and slope. Thus, the change in the LAPW basis must have the form of Eq. (25′); i.e., its value and slope go to zero at the sphere boundaries, a condition that determines $A^{a(1)}_{lmp,I}(\mathbf{k},\mathbf{G})$ uniquely as

$$A^{a(1)}_{lmp,I}(\mathbf{k},\mathbf{G}) = \frac{\left[u_{l\overline{p}}(S^a), \sum_{l'm'}\sum_{p'=0}^{1} A^a_{l'm'p'}(\mathbf{k},\mathbf{G}) u^{a(1)}_{l'm'p',I,lm}(S^a)\right]}{[u_{lp}(S^a), u_{l\overline{p}}(S^a)]} \tag{6}$$

for $p = \{0,1\}$ with $\overline{p} = 1 - p$, the Wronskian $[f(r),g(r)] = f(r)g'(r) - f'(r)g(r)$, and the radius $S^a$ of the MT sphere of atom $a$. For the special case of a spherical perturbation, Eq. (6) is identical to Eq. (31′).

Local orbitals[23] are additional basis functions that are completely confined within the MT spheres. They are employed to improve the description of semicore states or high-lying unoccupied states. A set of $2l + 1$ local orbitals of angular momentum $l$ and magnetic quantum number $m$ at atom $a$ is obtained from linearly combining three functions—$u_{lm0}(\mathbf{r})$, $u_{lm1}(\mathbf{r})$, and $u_{lmp}(\mathbf{r}) = u_{lp}(r)Y_{lm}(\mathbf{r})$ with $p \geqslant 2$ and an energy parameter $\epsilon_{lp} \neq \epsilon_l$—in such a way that the resulting function and its slope are zero at the MT sphere boundary. In analogy to the LAPW basis response, we find the linear change of the so-defined local orbitals from (a) the responses of the separate contributing functions according to Eqs. (2) and (3) [Eq. (2) for $p \geqslant 2$ ] and (b) the linear change of the expansion coefficients of the linear combination. As in the case of the LAPW matching coefficients, we determine the latter uniquely by requiring that the local-orbital response goes to zero in value and slope at the MT boundary and that it is orthogonal to the unperturbed local orbital.

The response of the basis functions, the *basis response*, is thus defined completely for general perturbations in the effective potential in the MT spheres. Linear combination with the wave-function coefficients yields $\tilde{\varphi}^{(1)}_{n\mathbf{k},I}(\mathbf{r})$ [Eq. (32′)]. The rest of the derivation is, as already mentioned in Ref. 18, independent of whether spherical or nonspherical perturbations are considered. Therefore, we only give the final result here,

$$\begin{aligned}\varphi^{(1)}_{n\mathbf{k},I}(\mathbf{r}) &= \sum_{\substack{n'\leqslant N\\ n'\neq n}} \left[\frac{\langle\varphi_{n'\mathbf{k}}|M_I|\varphi_{n\mathbf{k}}\rangle + \langle\varphi_{n'\mathbf{k}}|H - \epsilon_{n'\mathbf{k}}|\tilde{\varphi}^{(1)}_{n\mathbf{k},I}\rangle}{\epsilon_{n\mathbf{k}} - \epsilon_{n'\mathbf{k}}}\right]\varphi_{n'\mathbf{k}}(\mathbf{r}) \\ &\quad + \int d^3r' \left[\delta(\mathbf{r}-\mathbf{r}') - \sum_{n'\leqslant N}\varphi_{n'\mathbf{k}}(r)\varphi^*_{n'\mathbf{k}}(\mathbf{r}')\right]\tilde{\varphi}^{(1)}_{n\mathbf{k},I}(\mathbf{r}')\,.\end{aligned} \tag{7}$$

The first term is the usual sum-over-states expression of standard perturbation theory (SPT) with an additional term that we name *Pulay term* because it resembles the Pulay force in atomic force calculations.[24,25] It corrects for deviations of the calculated single-particle wave functions $\varphi_{n\mathbf{k}}(\mathbf{r})$ from the exact eigenstates. These deviations occur, especially for empty states at high energies, due to the incompleteness of the basis set.[26] The last term, numerically much more important than the Pulay term, contains in the square brackets a projection operator onto the orthogonal space. Thus, this term, which we call *basis-response (BR) term*, adds response contributions that lie outside the Hilbert space spanned by the basis set or, more specifically, the space spanned by the $N$ wave functions. We will later see that these contributions are substantial. This concludes the definition of the IBC. It is easy to see that the Pulay and basis-response terms vanish in the (theoretical) case of a complete basis (and $N = \infty$).

### B. Core-state response

In the FLAPW method, the core states are eigensolutions of an atomic problem for the spherical part of the effective potential inside the MT sphere including the $-Z/r$ Coulomb potential. The wave functions are thus determined as solutions to the Dirac equation with atomic boundary conditions. In

Ref. 18, we calculated the core response to a spherical perturbation directly from the finite difference of the perturbed and the unperturbed solution to the Dirac equation. However, given the spherical core solver at hand, this approach cannot be applied to nonspherical perturbations. Instead, we seek solutions of the perturbed Dirac equation, for which we employ the scalar-relativistic approximation for simplicity. For the general case of a nonspherical perturbation, this leads to a response in the form of Eq. (1), where $l$ and $m$ then correspond to the angular momentum and magnetic quantum number of the core state, and $p$ can be taken as the principal quantum number. The radial functions obey inhomogeneous differential equations similar to Eq. (2), where one would have to add the principal quantum number as an index to the radial functions and energies. In this sense, what we termed basis response above already yields the exact response of the core states, and no SPT and Pulay term is required. The only difference is that the radial differential equations are to be solved under the additional boundary condition that the core-state response approaches zero for $r \to \infty$.

For a given core state with quantum numbers $l$ and $m$, a given perturbation $M_I(\mathbf{r})$ with $I = (a,P,L,M)$ and a given $l'm'$ channel of the response [Eq. (1)], we enforce this boundary condition by a shooting approach, i.e., by performing both outward and inward integrations.[27] The former starts at the first numerical radial mesh point $r_{\min}$, which is very close to the nucleus ($r = 0$), and the latter starts at a large distance $r_{\max}$ (typically $r_{\max} = 20\,a_0$ with Bohr's atomic radius $a_0$) from the nucleus. Both end at the classical turning point $r_{\mathrm{TP}}$ defined by $[l(l+1)]/(2r_{\mathrm{TP}}^2) + V_{\mathrm{eff}}(r_{\mathrm{TP}}) = \epsilon_c$ with the core-state energy $\epsilon_c$. Employing zero initial values we construct two special solutions of the inhomogeneous differential equation, $\{p_{\mathrm{out}}(r),q_{\mathrm{out}}(r)\}$ and $\{p_{\mathrm{in}}(r),q_{\mathrm{in}}(r)\}$, where $p(r)/r$ and $q(r)/cr$ are the relativistic large and small component, respectively. Then, two homogeneous solutions $\{p_{\mathrm{out}}^{\mathrm{hom}}(r),q_{\mathrm{out}}^{\mathrm{hom}}(r)\}$ and $\{p_{\mathrm{in}}^{\mathrm{hom}}(r),q_{\mathrm{in}}^{\mathrm{hom}}(r)\}$ are obtained by setting $p_{\mathrm{out}}^{\mathrm{hom}}(r_{\min})$ and $p_{\mathrm{in}}^{\mathrm{hom}}(r_{\max})$ to arbitrary finite values, while $q_{\mathrm{out}}^{\mathrm{hom}}(r_{\min})$ and $q_{\mathrm{in}}^{\mathrm{hom}}(r_{\max})$ follow from the relations $\lim_{r\to 0} q(r)/p(r) = \{[1 + l'(l'+1) - (Z/c)^2]^{1/2} - 1\}c^2/Z$ and $\lim_{r\to\infty} q(r)/p(r) = -\{-(E/2)/(1 + E/2c^2)\}^{1/2}$.[28–30] The two sets of solutions are matched at $r_{\mathrm{TP}}$, giving two linear equations $p_{\mathrm{out}}(r_{\mathrm{TP}}) + a p_{\mathrm{out}}^{\mathrm{hom}}(r_{\mathrm{TP}}) = p_{\mathrm{in}}(r_{\mathrm{TP}}) + b p_{\mathrm{in}}^{\mathrm{hom}}(r_{\mathrm{TP}})$ and $q_{\mathrm{out}}(r_{\mathrm{TP}}) + a q_{\mathrm{out}}^{\mathrm{hom}}(r_{\mathrm{TP}}) = q_{\mathrm{in}}(r_{\mathrm{TP}}) + b q_{\mathrm{in}}^{\mathrm{hom}}(r_{\mathrm{TP}})$, from which $a$ and $b$ are determined. In the case $l = l'$ the two equations become linearly dependent, and the solution is unique only up to a multiple of the core-state eigenfunction. To fix the solution, we require it to be orthogonal to the core eigenfunction. On the contrary, for $l \neq l'$ no regular homogeneous solution can exist that is continuous and continuously differentiable over the whole range of radii (since there is no eigenstate in the $l'$ channel with the same eigenvalue). So, the solution of the linear equations is unique in this case.

The so-obtained function, $p_{\mathrm{out}}(r) + a p_{\mathrm{out}}^{\mathrm{hom}}(r)$ for $r \leqslant r_{\mathrm{TP}}$ and $p_{\mathrm{in}}(r) + b p_{\mathrm{in}}^{\mathrm{hom}}(r)$ for $r > r_{\mathrm{TP}}$ [analogously for $q(r)$], then solves the inhomogeneous differential equation, is continuous and continuously differentiable over the whole range of radii, and goes to zero at infinity. For spherical perturbations the present approach and the finite-difference method proposed in Ref. 18 yield identical results (up to numerical accuracy) when the scalar-relativistic approximation is used in both. The scalar-relativistic approximation for the response has been tested against the Dirac response for spherical perturbations and the differences were insignificant for all materials considered so far.

## III. APPLICATION TO EXX-OEP

As in Ref. 18, we apply the IBC to the OEP equation [Eq. (4′)], which involves two response functions, one for the electron density and one for the KS single-particle states. With the results of the previous section, the former is given by Eq. (36′), while the latter combines with the EXX functional to a corrected expression for the right-hand side of the OEP equation given by Eq. (37′).

To demonstrate the performance of the IBC, we calculate the antiferromagnetic (AFM-II, i.e., ferromagnetic (111) planes are coupled antiferromagetically along the [111] direction) bulk phase of NiO in the NaCl structure with four atoms in the unit cell. In this electronically complex material the localized Ni $3d$ states are only partially occupied: Due to the crystal field the $3d$ states are split into three occupied $t_{2g}$ and two empty $e_g$ states in one spin channel,[31] while the $3d$ shell of the other spin channel is completely filled. This partial $3d$ occupation gives rise to a pronounced anisotropy in the electron density distribution around the Ni atoms and, as a consequence, also in the calculated optimized effective potential $V_{\mathrm{x}}^{\sigma}(\mathbf{r})$, where $\sigma$ is the spin quantum number. Thus, nonspherical terms in $V_{\mathrm{x}}^{\sigma}(\mathbf{r})$ play a crucial role. The restriction of the IBC to spherical perturbations, while successful in other materials, turns out to be inadequate, and the generalization of the IBC is absolutely essential.

The calculations are performed at the experimental lattice constant of $7.882\,a_0$ and with LAPW cutoff values $G_{\max} = 4.1\,a_0^{-1}$ and $l_{\max} = 8$ for the linear and angular momenta, respectively. For the mixed product basis we employ $G'_{\max} = 3.0\,\mathrm{a}_0^{-1}$ and $L_{\max} = 4$.[22,32] The Ni $3s$ and $3p$ semicore states are described as valence electrons by local orbitals. The Brillouin zone (BZ) is sampled with a $2 \times 2 \times 2$ and a $4 \times 4 \times 4$ **k**-point set in the test calculations and the calculations for Table II, respectively. We consider the convergence of the LAPW basis set only in the MT spheres, while the convergence in terms of $G_{\max}$ is much less demanding in practice and will not be discussed any further. We improve the description in the MT spheres by adding local orbitals with energy parameters in the unoccupied spectrum; we add from one ($n_{\mathrm{LO}} = 1$) up to six ($n_{\mathrm{LO}} = 6$) sets of local orbitals per atom and $lm$ channel with $0 \leqslant l \leqslant 6$,[32] corresponding to 196 up to 1176 additional functions.

Figure 1 shows the trace of the density response function $\chi_s$ of NiO [$\mathrm{tr}(\chi_s^{\uparrow})$ and $\mathrm{tr}(\chi_s^{\downarrow})$ are identical due to the antiferromagnetic structure] in terms of the parameter $n_{\mathrm{LO}}$. The top axis gives the corresponding size of the basis set. All calculated states are included in the sums of Eq. (36′). We omit the response of the core states (Sec. II B) as they would merely shift the curves downwards. We distinguish between elements corresponding to functions without (solid lines, left scale) and with spherical symmetry (dashed lines, right scale) as well as between the SPT term, the BR term, the Pulay term, and their sum. The inset shows the latter on a finer scale. We see

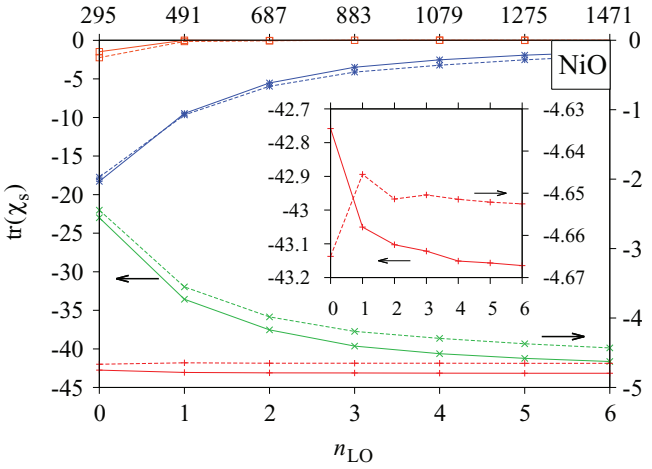


FIG. 1. (Color online) Convergence of the trace of the density response matrix $\chi_s$ for antiferromagnetic NiO as a function of $n_{LO}$, which determines the size of the basis set given in the top axis. The trace is over the spherical (dashed lines, right scale) and nonspherical MT parts of $\chi_s$ (solid lines, left scale). The (green) crosses, (blue) stars, and (orange) squares correspond to the SPT, BR, and Pulay terms, respectively. The sum of all terms is shown as (red) pluses.

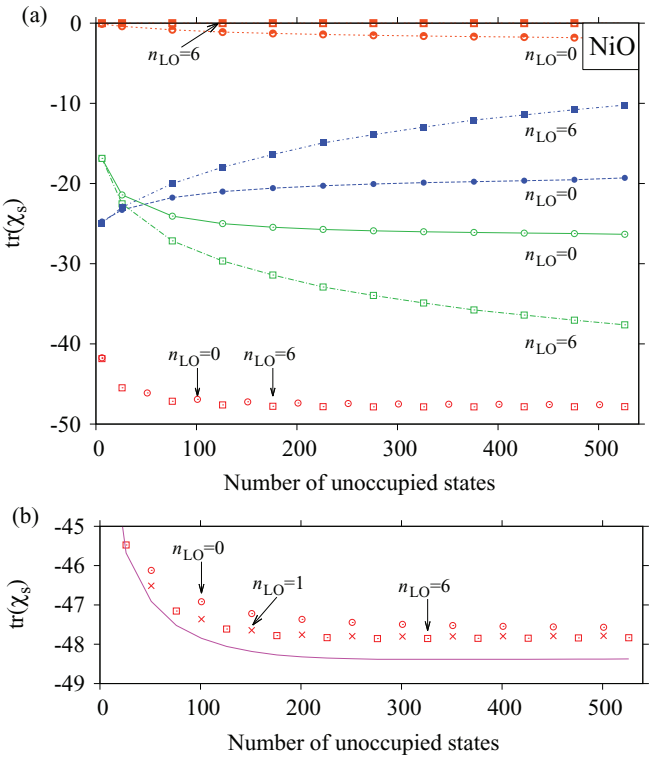


FIG. 2. (Color online) (a) Convergence of the SPT [(green) open symbols], BR [(blue) solid symbols], and Pulay terms [(orange) half-solid symbols] of the MT part of tr($\chi_s$) as well as their sum [(red) open symbols] as a function of the number of unoccupied states. Circles and squares are used to distinguish the cases $n_{LO} = 0$ and 6. Figure (b) shows in addition results for $n_{LO} = 1$ [(red) crosses] and the total trace including the interstitial part [(magenta) solid line]. (We note that for these calculations the reciprocal cutoff value was increased to $G_{max} = 5.1\, a_0^{-1}$ to generate enough states.)

that the nonspherical part of $\chi_s$ exhibits the same convergence behavior as the spherical part; also compare the corresponding plot for ScN in Ref. 18. The SPT term, the standard expression usually used in linear response calculations, shows a very slow convergence with respect to the size of the basis set. The IBC accounts for nearly 100% for what is missing in the SPT term as evidenced by the lines representing the sums of all terms, which appear to be nearly constant on the scale of the graph; also compare the finer scale in the insets. A very precise response function is achieved already with the conventional LAPW basis ($n_{LO} = 0$). We also see that the spherical and the nonspherical parts of $\chi_s$ converge equally fast with respect to the basis-set size. Without showing further results, we note that the right-hand side of the OEP equation benefits from the IBC in a similar way.

So far, all calculated states (as many as there are basis functions) have been considered in Eq. (36′), i.e., all occupied and unoccupied states. Now, we treat the number of unoccupied states as a convergence parameter and examine for fixed basis sets the convergence behavior of the trace tr($\chi_s$). Figure 2(a) shows the corresponding SPT, Pulay, and BR terms and their sum including spherical and nonspherical elements for $n_{LO} = 0$ and $n_{LO} = 6$. Similarly to Fig. 3 in Ref. 18, the sum converges very rapidly as a function of the number of empty states. The slight zigzag behavior of the sum between the circles and squares corresponds to the difference in values for $n_{LO} = 0$ and $n_{LO} = 6$ in Fig. 1. Figure 2(b) shows these curves on a finer scale including results for $n_{LO} = 1$ for comparison. Up to now, we have only shown results for that part of $\chi_s$ that corresponds to perturbations in the MT spheres. These are the perturbations for which the IBC is defined. The response to perturbations in the interstitial, on the other hand, is only covered by the SPT term. Fortunately, the interstitial response exhibits a favorable convergence behavior with respect to the unoccupied states, as shown by the solid line in Fig. 2(b), so that good convergence is achieved for the whole of the density response matrix.

We now turn to the local exchange potential $V_x^\sigma(\mathbf{r})$ obtained as the solution of the OEP equation [Eq. (4′)]. Figure 3 shows the spin-up and spin-down potential at the Ni site. The former is lower in energy than the latter, which favors occupation of spin-up states at this Ni atom. The local magnetization thus points in the direction of spin up. In the (111) plane [Fig. 3(a)], in which the Ni atoms order ferromagnetically, the potential is circularly symmetric (on the scale of the diagram), which is due to the symmetry of the crystal and magnetic structure. In the spin-down channel, only the $t_{2g}$ states are filled, while the $e_g$ states are empty leading to the circularly symmetric potential on the (111) plane when we disregard for the moment contributions from higher angular momenta ($l > 2$). The antiferromagnetic order breaks the cubic symmetry of the lattice. But since it is along the [111] direction, it leaves the symmetry in the (111) plane intact, and the potential remains symmetric. The same applies to the spin-up channel, in which the whole $3d$ shell is occupied. Very slight deviations from circular symmetry, not visible on the scale of the diagram, arise from including angular momenta beyond $l = 2$. In the $(\bar{1}10)$ plane, which is perpendicular to the ferromagnetic planes, we still find an approximate circular

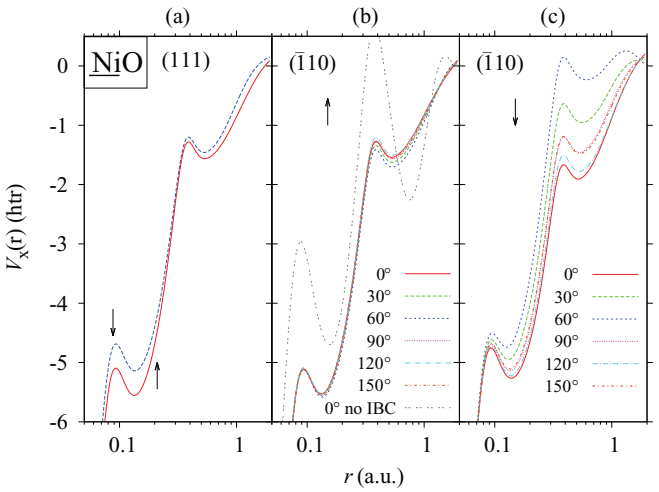


FIG. 3. (Color online) Local exchange potential $V_x^\sigma(\mathbf{r})$ of antiferromagnetic NiO at the Ni atom (a) in the ferromagnetically ordered (111) plane as well as (b),(c) in the perpendicular $(\bar{1}10)$ plane for the two spin channels, where the up spin is in the direction of local magnetization. While $V_x^\sigma(\mathbf{r})$ is approximately circularly symmetric in (a) and (b), it shows a pronounced direction dependence in (c). Figure (b) also shows $V_x^\sigma(\mathbf{r})$ calculated without the IBC. (See Fig. 4.)

symmetry of the potential in the spin-up channel [Fig. 3(b)], which—together with the symmetry seen in (a)—makes the spin-up potential nearly isotropic. However, in contrast to the (111) plane, the direction dependence becomes clearly visible in the diagram. A much stronger effect is, however, seen when the 3*d* shell is not completely filled. Figure 3(c) shows the spin-down potential for several directions in the plane $(\bar{1}10)$ from 0° [perpendicular to the (111) plane] over 90° [parallel to the (111) plane] to 150°; the direction 180° is identical to 0° owing to the twofold rotational symmetry. There is a clear difference between the potential along the ferromagnetic plane (90°) and the one that connects to the neighboring Ni plane with opposite magnetization (0°). We also observe a strong influence of the immediate atomic environment: there is a maximum in the direction of the nearest oxygen atom at around 60° and a smaller maximum in the direction of the oxygen atom of the neighboring plane at around 150° (see Fig. 4). This

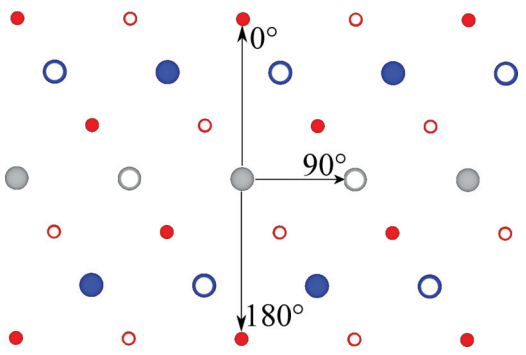


FIG. 4. (Color online) $(\bar{1}10)$ plane of NiO; Ni atoms are shown as the large bright (grey) and dark (blue) balls for spin up and down, respectively; the O atoms are shown as small (red) balls. The open balls refer to atoms located on the neighboring plane. The 0°, 90°, and 180° directions corresponding to Fig. 3 are indicated.

strong direction dependence of the spin-down potential makes the generalization of the IBC to nonspherical perturbations absolutely necessary for obtaining a well converged potential already with the conventional LAPW basis ($n_{\mathrm{LO}} = 0$). In Fig. 3(b) we indicate the potential calculated without the IBC as a comparison. It exhibits unphysically strong oscillations, especially at the positions of the intershell humps, pointing at an underconverged density response function.

The augmentation of the LAPW basis by local orbitals leads to changes of the EXX potential which would be (nearly) indistinguishable on the scale of Fig. 3. Between $n_{\mathrm{LO}} = 0$ and $n_{\mathrm{LO}} = 1$ maximal absolute changes of the potential of 0.06 Htr occur in the vicinity of the intershell humps. These correspond to a relative change of 3%, demonstrating that the generalized IBC leads to a stable and physical EXX potential already at the conventional LAPW basis set with $n_{\mathrm{LO}} = 0$.

Finally, we analyze the convergence of the EXX transition energies for NiO as a function of the quality of the LAPW basis set. In particular, we focus on the KS transitions between the highest occupied and the lowest unoccupied state at the Γ, L, and F points of the rhombohedral BZ of NiO. The rhombohedral BZ with its high-symmetry points is illustrated in Fig. 3 of Ref. 33. We show in Table I PBE and EXX KS transition energies as a function of the number of local orbitals $n_{\mathrm{LO}}$ added to the LAPW basis for each atom in all *lm* channels with $0 \leqslant l \leqslant 6$. In the case of the EXX functional we moreover distinguish two cases: (a) only the SPT term is taken into account in the computation, and (b) the generalized IBC is employed.

We perform a single EXX-OEP iteration starting from the self-consistent PBE potential for each basis set, characterized by the number of local orbitals added. Then, in order to eliminate possible linearization errors of the basis,[34] the OEP Hamiltonian is diagonalized with the most accurate basis set ($n_{\mathrm{LO}} = 6$) so that the variations in the transition energies can be solely attributed to the precision of the EXX potential.

In accordance with the previous analysis, the transition energies exhibit a very slow convergence in case (a). Between $n_{\mathrm{LO}} = 0$ and $n_{\mathrm{LO}} = 6$, for example, the $\Gamma \rightarrow \Gamma$ transition energy changes by as much as 2.402 eV. Not even with $n_{\mathrm{LO}} = 6$ can we achieve satisfactory convergence. With the generalized IBC, however, the KS transition energies are already converged at $n_{\mathrm{LO}} = 0$ to a precision of 58 meV. Adding one set of local orbitals yields a transition energy that deviates from the fully converged one only by 15 meV. In fact, by comparing with the first column of the table, we find that this convergence behavior is similar in quality to that of calculations with the much simpler semilocal PBE functional.

As already mentioned, the local exchange potential of NiO is strongly nonspherical around the Ni atom, which is a consequence of the partially filled 3*d* states. In fact, if we restrict $V_x^\sigma(r)$ to be spherical by setting $L_{\max} = 0$, we obtain a metal instead of a large-gap semiconductor in EXX-OEP. For the same reason, the IBC restricted to spherical perturbations (corresponding to the formulation of Ref. 18) even worsens the results with respect to SPT because of an imbalance between an underconverged nonspherical part of $V_x^\sigma(r)$ and a well converged spherical part. This imbalance pushes the system towards a metallic ground state. This is in contrast to electronically less complex materials, such as rocksalt ScN, where the X→X transition energy changes

TABLE I. One-shot EXX KS band transition energies for antiferromagnetic NiO for LAPW basis sets augmented by up to six local orbitals ($n_{\mathrm{LO}} = 6$) per atom and $lm$ channel with $0 \leqslant l \leqslant 6$. The (absolute) change $\Delta$ of the transition energies between $n_{\mathrm{LO}} = 0$ and $n_{\mathrm{LO}} = 6$ is shown in the last row of the table. Fully converged results are given in Table II.

| NiO | PBE | | | EXX | | | | | |
|---|---|---|---|---|---|---|---|---|---|
| | | | | (a) SPT | | | (b) SPT + IBC | | |
| $n_{\mathrm{LO}}$ | $\Gamma \to \Gamma$ | L → L | F → F | $\Gamma \to \Gamma$ | L → L | F → F | $\Gamma \to \Gamma$ | L → L | F → F |
| 0 | 2.343 | 1.558 | 2.196 | 5.952 | 9.132 | 9.194 | 3.395 | 7.357 | 6.825 |
| 1 | 2.362 | 1.598 | 2.220 | 4.817 | 8.782 | 8.449 | 3.373 | 7.411 | 6.871 |
| 2 | 2.363 | 1.602 | 2.221 | 4.159 | 8.270 | 7.781 | 3.373 | 7.427 | 6.875 |
| 3 | 2.366 | 1.608 | 2.225 | 3.763 | 7.856 | 7.338 | 3.357 | 7.414 | 6.860 |
| 4 | 2.366 | 1.608 | 2.225 | 3.659 | 7.746 | 7.205 | 3.361 | 7.417 | 6.866 |
| 5 | 2.366 | 1.609 | 2.226 | 3.575 | 7.644 | 7.103 | 3.359 | 7.415 | 6.864 |
| 6 | 2.367 | 1.610 | 2.226 | 3.550 | 7.604 | 7.072 | 3.358 | 7.415 | 6.862 |
| $\Delta$ | 0.024 | 0.052 | 0.030 | 2.402 | 1.528 | 2.122 | 0.037 | 0.058 | 0.037 |

by 220 meV (16 meV) between $n_{\mathrm{LO}} = 0\,(1)$ and $n_{\mathrm{LO}} = 6$ if only the SPT is employed. Including the spherical IBC, the corresponding difference is reduced to 36 meV (5 meV), whereas the generalized IBC reduces the difference further to 4 meV (<1 meV).

## IV. DISCUSSION OF NiO

In this section, we discuss the electronic structure of antiferromagnetic NiO as obtained with the EXX functional and compare it to corresponding PBE and experimental results.

The most obvious result is an opening of the KS band gap from 1.00 eV in the PBE approximation to 3.42 eV in EXX. Including correlation[35] on the level of LDA opens the gap further by 0.23 eV. The EXX as well the EXX + LDAc (EXXc) gaps are much closer to the experimental values of 4.0 eV[36] and 4.3 eV[37] than the PBE value. In comparison to the pseudopotential EXXc calculation of Ref. 38, our all-electron KS gap is smaller by 0.45 eV. We note that the KS gaps do not include the derivative discontinuity of the exchange potential (see Refs. 9 and 39 for a detailed discussion). Furthermore, we observe an increase of the spin magnetic moment. In fact, the EXX moment of 1.90 $\mu_B$ lies very close to the experimental magnetic moment (cf. Table II).

Figure 5 shows the KS band structure and density of states (DOS) calculated with the PBE and EXX functional. We distinguish between the two spin channels, where spin up again refers to the direction of the magnetization of a given Ni atom. We first focus on the occupied valence states. While in the PBE calculation the spin-up and spin-down DOS of the occupied Ni $3d$ states overlap strongly, they are clearly separated by a gap of 0.8 eV in the EXX approach. The highest occupied states in the EXX approach, which reside in the spin-down channel, exhibit nearly pure Ni $3d$ character. In contrast, these states are a mixture of spin-up and spin-down Ni $3d$ and O $2p$ states in the PBE calculation. The O $2p$ states stretch out over the energy range from −8 eV to 0 eV with small contributions even in the conduction states, whereas they are almost completely confined within a region from −8 eV to −1.7 eV in the EXX approach. The prominent peak at about −7.1 eV in the EXX spectrum formed by the flat spin-down $t_{2g}$ bands, which is seen in experiment (see below), is completely absent in the PBE calculation.

The PBE and EXX calculations predict valence band maxima at different positions in the BZ. While the maximum lies on the BZ path between the Γ and F points in the case of

TABLE II. Fundamental band gap $E_{\mathrm{gap}}$ (eV) and spin magnetic moment $M_{\mathrm{spin}}$ ($\mu_B$) of antiferromagnetic NiO (AFM-II) calculated with the VWN, PBE, EXX, and EXXc functionals and experimental values. (Note that the experimental magnetic moment also contains the orbital contribution.[40]) The values in brackets are taken from a pseudopotential plane-wave study.[38] All calculations are performed with a $4 \times 4 \times 4$ **k**-point set.

| | VWN | PBE | EXX | EXXc | Expt. |
|---|---|---|---|---|---|
| $E_{\mathrm{gap}}$ | 0.46 | 1.00 | 3.42 | 3.65 (4.10) | 4.0[a], 4.3[b] |
| $M_{\mathrm{spin}}$ | 1.27 | 1.41 | 1.90 | 1.90 (1.89) | 1.81[c], 1.90[d] |

[a]Reference 36.
[b]Reference 37.
[c]Reference 41.
[d]Reference 42.

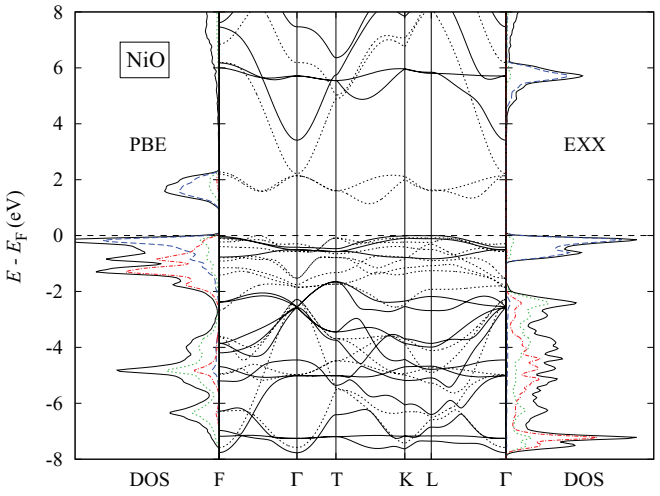


FIG. 5. (Color online) PBE (dashed black lines) and EXX (solid black lines) KS band structure and density of states (DOS) (in units of states/eV) for NiO. The contributions of the spin-up and spin-down Ni $3d$ states to the total DOS (black line) are shown as the (red) dot-dashed and (blue) dashed lines, respectively, and the partial DOS for O $2p$ as the (green) dotted line.

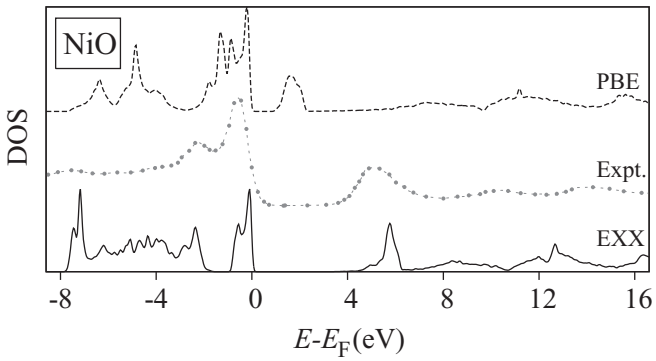


FIG. 6. Comparison of the EXX (solid line) and PBE (dashed line) DOS of NiO with experimental spectra from x-ray photoemission spectroscopy (XPS) and bremsstrahlung isochromat spectroscopy (BIS) (dashed line with dots) taken from Ref. 37.

the PBE functional, it is found in the vicinity of the $L$ point for the EXX functional. Similarly, the conduction band minimum differs in both approaches. For the PBE functional it is located on the BZ path between the T and K points, while it lies in the center of the BZ for the EXX approach.

We observe that the opening of the band gap is accompanied by a significant change of the lowest conduction bands. While in the PBE approximation the lowest unoccupied band are formed mainly from spin-down Ni 3$d$ states with a parabolic band of dominant Ni 4$s$ character following above them, the band ordering is reversed in the EXX band structure. The lowest unoccupied state exhibits Ni 4$s$ character, and the spin-down Ni 3$d$ bands appear at higher energies. We point out that the discussed characteristics of the all-electron EXX band structure and DOS are in very good agreement with previous pseudopotentials results (cf. Fig. 5 of Ref. 38).

In Fig. 6, we compare the PBE and EXX DOS with the experimental spectrum of NiO. The experimental spectrum of the occupied states exhibits a double peak structure with discrete peaks at $-0.7$ eV and $-2.4$ eV and a shallow peak at $-7.9$ eV. Both the double peak structure and the peak at $-7.9$ eV are reproduced by the EXX calculation. From the PBE calculation, on the other hand, one would expect a single broad peak below the Fermi energy and at least one additional peak at about $-4.8$ eV, which is in contradiction to experiment. The experimental spectrum of the unoccupied states measured by inverse photoemission shows three peaks between 4 eV and 16 eV above the Fermi energy. The energetic position of the first peak is strongly underestimated in the PBE calculation. Due to the opening of the band gap by the EXX functional (see above) the position of the first peak is shifted to a higher energy so that it is in good agreement with the peak found in experiment, albeit slightly overestimated. The two other experimental peaks, while absent in PBE, are reproduced by EXX, however at smaller energies.

## V. CONCLUSIONS

In this work, we extended the incomplete-basis-set correction (IBC), introduced in Ref. 18 for the calculation of all-electron response functions, to nonspherical perturbations, corresponding to response matrix elements that involve nonspherical functions. The main ingredient of the IBC is the response of the basis functions to perturbations in the effective potential. This response is constructed from the solutions of inhomogeneous differential equations in the muffin-tin (MT) spheres, which can be understood as radial Sternheimer equations. Rather than by summing over unoccupied states, these solutions are obtained straightforwardly by radial integration, in a similar way as the construction of the MT basis functions themselves.

In contrast to the simpler case of spherical perturbations in the effective potential, the $lm$ channels couple in the case of nonspherical perturbations, and the basis response no longer has pure angular character; it is given by a linear combination over different angular momenta. Likewise, the response of the core electrons to a nonspherical perturbation is calculated solving the scalar-relativistic Sternheimer equation by a shooting method to obey the proper boundary conditions. We note that the full-potential IBC is a rather general approach that can also be applied to calculate the response due to a nonspherical perturbation caused by an external potential, even in all-electron methods where the potential is restricted to be spherical.

We have applied the generalized IBC to the exact-exchange (EXX) optimized-effective-potential (OEP) approach of Kohn-Sham (KS) density-functional theory. The generalization of the IBC is crucial in systems that exhibit strongly angular dependent electron densities around the nuclei. As an example, we have discussed antiferromagnetic NiO, whose 3$d$ shell is only partially occupied. The generalized IBC leads to a converged KS density response function, a converged EXX potential, and converged KS transition energies at much smaller LAPW basis sets than without the correction. The EXX-OEP calculations become numerically very stable, and the converged EXX potential is obtained at a much smaller computational cost. Basis-set convergence is realized as fast as in conventional density-functional theory calculations using standard or semilocal functionals.

In comparison to the PBE functional, the EXX-OEP approach leads to an opening of the band gap and an enhancement of the spin magnetic moment of antiferromagnetic NiO so that both values are in much better agreement with experiment. Moreover, the EXX density of states shows a good agreement to experimental spectra obtained from direct and inverse photoemission experiments.

*m.betzinger@fz-juelich.de

[1]P. Hohenberg and W. Kohn, Phys. Rev. **136**, B864 (1964).
[2]W. Kohn and L. J. Sham, Phys. Rev. **140**, A1133 (1965).
[3]C. Fiolhais, F. Noguiera, and M. A. L. Marques, eds., *A Primer in Density Functional Theory*, Lecture Notes in Physics Vol. 620 (Springer, Heidelberg, 2003).

[4]S. Baroni, S. de Gironcoli, A. Dal Corso, and P. Giannozzi, Rev. Mod. Phys. **73**, 515 (2001).
[5]X. Ren, P. Rinke, C. Joas, and M. Scheffler, J. Mater. Sci. **47**, 7447 (2012).
[6]A. Heßelmann and A. Görling, Mol. Phys. **109**, 2473 (2011).
[7]W. G. Aulbur, L. Jönsson, and J. W. Wilkins, Solid State Phys. **54**, 1 (1999).
[8]F. Aryasetiawan and O. Gunnarsson, Rep. Prog. Phys. **61**, 237 (1998).
[9]S. Kümmel and L. Kronik, Rev. Mod. Phys. **80**, 3 (2008), and references therein.
[10]A. Görling, J. Chem. Phys. **123**, 062203 (2005).
[11]H. L. Skriver, *The LMTO Method* (Springer, New York, 1984).
[12]M. Methfessel, M. van Schilfgaarde, and R. Casali, in *Electronic Structure and Physical Properies of Solids*, edited by H. Dreysse, Lecture Notes in Physics Vol. 535 (Springer, Berlin, 2000), pp. 114–147.
[13]E. Wimmer, H. Krakauer, M. Weinert, and A. J. Freeman, Phys. Rev. B **24**, 864 (1981).
[14]M. Weinert, E. Wimmer, and A. J. Freeman, Phys. Rev. B **26**, 4571 (1982).
[15]H. J. F. Jansen and A. J. Freeman, Phys. Rev. B **30**, 561 (1984).
[16]P. J. H. Denteneer and W. van Haeringen, J. Phys. C: Solid State Phys. **18**, 4127 (1985).
[17]W. E. Pickett, Comput. Phys. Rep. **9**, 115 (1989).
[18]M. Betzinger, C. Friedrich, A. Görling, and S. Blügel, Phys. Rev. B **85**, 245124 (2012).
[19]R. M. Sternheimer, Phys. Rev. **96**, 951 (1954); **107**, 1565 (1957); **115**, 1198 (1959); **183**, 112 (1969).
[20]T. Kotani and M. van Schilfgaarde, Solid State Commun. **121**, 461 (2002).
[21]F. Aryasetiawan and O. Gunnarsson, Phys. Rev. B **49**, 16214 (1994).
[22]C. Friedrich, A. Schindlmayr, and S. Blügel, Comput. Phys. Commun. **180**, 347 (2009).
[23]D. Singh, Phys. Rev. B **43**, 6388 (1991).
[24]J. M. Soler and A. R. Williams, Phys. Rev. B **40**, 1560 (1989).
[25]R. Yu, D. Singh, and H. Krakauer, Phys. Rev. B **43**, 6411 (1991).
[26]In Eq. (7), we have omitted the symmetric expression $\langle\tilde{\varphi}^{(1)}_{n'\mathbf{k},I}|H-\epsilon_{n\mathbf{k}}|\varphi_{n\mathbf{k}}\rangle$, which is negligible for low-lying states $\varphi_{n\mathbf{k}}$, in particular for the occupied states.
[27]G. D. Mahan and K. R. Subbaswamy, *Local Density Theory of Polarizability* (Plenum, New York, 1990).
[28]J. Zabloudil, R. Hammerling, P. Weinberger, and L. Szunyogh, *Electron Scattering in Solid Matter*, Springer Series in Solid-State Sciences Vol. 147 (Springer-Verlag, Berlin, 2005).
[29]W. R. Johnson, *Atomic Structure Theory*, Lectures on Atomic Physics (Springer-Verlag, Berlin, 2007).
[30]O. Certik, J. E. Pask, and Jiri Vackar, Comput. Phys. Commun. **184**, 1777 (2013).
[31]The antiferromagnetic structure breaks the cubic symmetry, which leads to a slight lifting of degeneracies of the $t_{2g}$ and $e_g$ states.
[32]M. Betzinger, C. Friedrich, S. Blügel, and A. Görling, Phys. Rev. B **83**, 045105 (2011).
[33]J. E. Pask, D. J. Singh, I. I. Mazin, C. S. Hellberg, and J. Kortus, Phys. Rev. B **64**, 024403 (2001).
[34]G. Michalicek, M. Betzinger, C. Friedrich, and S. Blügel, Comput. Phys. Commun., doi: 10.1016/j.cpc.2013.07.002.
[35]S. H. Vosko, L. Wilk, and M. Nusair, Can. J. Phys. **58**, 1200 (1980).
[36]S. Hüfner, J. Osterwalder, T. Riesterer, and F. Hulliger, Solid State Commun. **52**, 793 (1984).
[37]G. A. Sawatzky and J. W. Allen, Phys. Rev. Lett. **53**, 2339 (1984).
[38]E. Engel and R. N. Schmid, Phys. Rev. Lett. **103**, 036404 (2009).
[39]M. Städele, M. Moukara, J. A. Majewski, P. Vogl, and A. Görling, Phys. Rev. B **59**, 10031 (1999).
[40]V. Fernandez, C. Vettier, F. de Bergevin, C. Giles, and W. Neubeck, Phys. Rev. B **57**, 7870 (1998).
[41]H. A. Alperin, J. Phys. Soc. Jpn. Suppl. B **17**, 12 (1962).
[42]A. K. Cheetham and D. A. O. Hope, Phys. Rev. B **27**, 6964 (1983).